



GLOBAL JOURNAL OF RESEARCHES IN ENGINEERING: D
AEROSPACE SCIENCE
Volume 23 Issue 1 Version 1.0 Year 2023
Type: Double Blind Peer Reviewed International Research Journal
Publisher: Global Journals
Online ISSN: 2249-4596 & Print ISSN: 0975-5861

Experiment-based Internal Ballistics Simulation of Dual-Thrust Solid Rocket Motors

By Alaa R Abdel Gawad, Liang Guozhu & Mahmoud Y. M. Ahmed

Beihang University (BUAA)

Abstract- A key aspect to a successful simulation of the flow inside the Dual Thrust Solid Rocket Motor (DTSRM) is the proper definition of boundary and operating conditions as well as fluid properties. The experimental pressure-time curve was analyzed and divided into five regimes to be used as inputs for numerical simulations to understand the flow features inside an experimental DTSRM motor and to estimate its thrust. The entire motor operation time from ignition to tail-off was examined including two steady-state phases; boost and sustain, and three transient phases, ignition, boost-sustain transition, and tail-off. The grain burnback analysis was carried out to obtain the computational domain for each simulation. The operating pressure for each simulation is defined as equal to the measured chamber pressure which was measured at the head end of the motor. The results confirmed the capabilities of simulations to explore the flowfield inside the motor and to predict its thrust with remarkable accuracy of less than 5% relative to the experimental measurements in lieu of analytical calculations that are more suited for preliminary calculations and only offer accuracy of about 15% relative to experimental measurements.

Keywords: dual-thrust solid rocket motor, internal ballistics, grain burnback, numerical simulation.

GJRE-D Classification: DDC Code: 519.2 LCC Code: QA273



Strictly as per the compliance and regulations of:



© 2023. Alaa R Abdel Gawad, Liang Guozhu & Mahmoud Y. M. Ahmed. This research/review article is distributed under the terms of the Attribution-NonCommercial-NoDerivatives 4.0 International (CC BYNCND 4.0). You must give appropriate credit to authors and reference this article if parts of the article are reproduced in any manner. Applicable licensing terms are at <https://creativecommons.org/licenses/by-nc-nd/4.0/>.

Experiment-based Internal Ballistics Simulation of Dual-Thrust Solid Rocket Motors

Alaa R Abdel Gawad ^α, Liang Guozhu ^σ & Mahmoud Y. M. Ahmed ^ρ

Abstract- A key aspect to a successful simulation of the flow inside the Dual Thrust Solid Rocket Motor (DTSRM) is the proper definition of boundary and operating conditions as well as fluid properties. The experimental pressure-time curve was analyzed and divided into five regimes to be used as inputs for numerical simulations to understand the flow features inside an experimental DTSRM motor and to estimate its thrust. The entire motor operation time from ignition to tail-off was examined including two steady-state phases; boost and sustain, and three transient phases, ignition, boost-sustain transition, and tail-off. The grain burnback analysis was carried out to obtain the computational domain for each simulation. The operating pressure for each simulation is defined as equal to the measured chamber pressure which was measured at the head end of the motor. The results confirmed the capabilities of simulations to explore the flowfield inside the motor and to predict its thrust with remarkable accuracy of less than 5% relative to the experimental measurements in lieu of analytical calculations that are more suited for preliminary calculations and only offer accuracy of about 15% relative to experimental measurements.

Keywords: dual-thrust solid rocket motor, internal ballistics, grain burnback, numerical simulation.

I. INTRODUCTION

The Dual Thrust Solid Rocket Motors (DTSRMs) are solid propellant rocket motors that have the capability of yielding a dual (step) thrust; a high thrust followed by a lower one. This boost-sustain feature finds applications in a variety of guided missiles. Boosting the missile allows it to swiftly accelerate to the nominal flight speed in a minimum uncontrolled flight time. The subsequent low thrust ensures near-zero acceleration to maintain the nominal flight speed (proper for control) for a maximum controlled flight time.

A dual thrust is achieved by different motor designs including single-chamber and single fixed nozzle, single-chamber and single variable nozzle, double-tandem chamber and single external nozzle, double-chamber and double nozzle configurations. Nonetheless, the simplest design is the one in which one chamber incorporating two grains of different configurations is used. This simplicity comes with motor operation complexity as it involves five different phases

including two steady-state phases and three transient phases (ignition, transition, and tail-off).

Understanding the SPRM operation is a crucial step in missile mission design. Experimental measurements of chamber pressures and motor thrust are perhaps the most reliable in defining the overall motor operation. Nevertheless, practice shows that variable thrust measurement of DTSRM may be troublesome due to variation in thrust level. While measuring pressure can be simply achieved, the use of two different load cells for the same motor may not be as simple. Analytical techniques based on solving internal ballistic relations may also be used to estimate the motor pressure and thrust. However, if it is sought to understand the flow behavior and explore its features along the motor, neither experimentation nor analytical technique is the right approach. Numerical simulation of the flow along the DTSRM gives a better understanding of the multiple flow features associated with the two levels of pressure including streamlines, pressure, temperature, density, and velocity variation along the motor which cannot be attained from experimental measurements or analytical calculations. In addition, both numerical simulations and analytical calculations have the advantages of higher flexibility and lower cost and risk compared with experimental measurements. Yet, numerical simulations have higher fidelity compared with analytic calculations. One key aspect of the successful simulation is the proper definition of operating and boundary conditions. Using accurate experiment-based inputs would indeed yield more reliable simulation results.

The use of numerical simulation via the computational fluid dynamics (CFD) approach to understand and analyze the flow field through solid-propellant rocket motors has been widely adopted [1-8]. Some researchers focused on the ignition transient phase [9-15] to investigate phenomena accompanied by starting transient such as internal flow choking, pre-ignition chamber dynamics, and boundary layer displacement. While some focused on quasi-steady-state and tail-off phases [16] to analyze the validity of performance prediction for parameters such as pressure, thrust, and nozzle throat variation. Pressure oscillation and acoustic instability taking place in the solid rocket were also addressed using numerical simulation [17-21]. Recently, more attention has been paid to using CFD in simulating solid rocket motors regression [22]. Li et al.

Author α: Ph.D. Candidate, School of Astronautics, Beihang University (BUAA), Beijing, China. e-mail: alaarabie@buaa.edu.cn

Author σ: Professor, School of Astronautics, Beihang University (BUAA), Beijing, China.

Author ρ: Ass. Professor, Aerospace Department, Military Technical College, Cairo, Egypt.

[23] presented an integrated framework for coupled simulation of internal fluid flow in a solid rocket motor and burning surface regression of propellant. Lin [24] developed an immersed boundary method to avoid the cumbersome re-meshing for simulating the coupling of gas flow and burning surface regression in solid rocket motors. Zou et al. [25] developed a numerical model to investigate the regression rate and the combustion process of a combined solid rocket motor for different grain inner diameters. Some advanced topics related to numerical simulation for solid rocket motors have been discussed. Han and Kim [26] examined the interaction between burning module, structure, and fluid inside solid rocket motors. Hemanth and Jyothi [27] simulated the flow inside a retro solid-propellant rocket motor.

The objective of the present work is to simulate the flow inside a DTSRM using computational fluid dynamics based on the pressure from experimental measurements to reflect the internal flow characteristics for the combustion chamber and nozzle together. The grain recession calculation was carried out to obtain the grain shapes along the whole motor burning time which represents the computational domain used in

simulations. The simulations will cover the whole burning time starting from ignition to tail-off obtaining all possible internal flow parameters. From these parameters, the internal ballistics of the case study DTSRM and the resulting thrust is calculated. In such cases, simulation results may be used to predict motor thrust with accuracy closer to experimental measurements compared with the analytical calculations.

II. EXPERIMENTAL MOTOR

For the present case study, a test solid rocket motor is adopted, Figure 1a with the pressure transducer adjusted at the head end of the motor. A tubular grain of two different inner diameters along the axis is used. The tubular grain is inhibited from the outer surface adjacent to the motor casing while it is allowed to burn from all other surfaces, Figure 1b. The solid propellant composition includes ammonium perchlorate, Aluminum powder, and HTPB with the percentages shown in Table 1. The burning law for the propellant is defined as:

$$r = 2.68 \times 10^{-4} p^{0.2101} \quad (1)$$

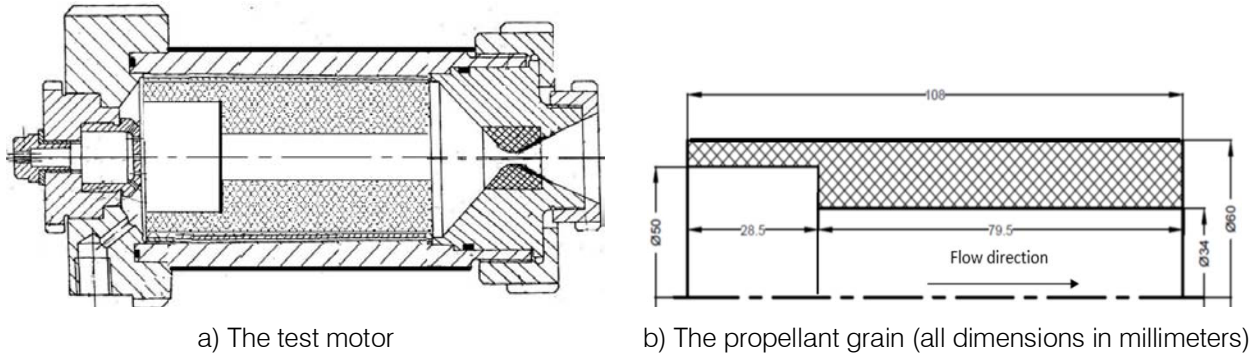


Figure 1: The experimental motor and the propellant grain

Table 1: Propellant Ingredient

	AP	Al	HTPB
Chemical formula	NH_4ClO_4	Al	$C_{7.09}H_{10.86}O_{0.227}$
Weight percentage[%]	69	17	14
Enthalpy [kcal/mol]	-70.69	0	-14.64

III. METHODOLOGY

For sake of numerical simulation, the pressure ~ time curve from experimental measurements was divided into five regimes namely, ignition transient phase, boost steady phase, transition transient phase, sustain steady phase, and tail-off transient phase as shown in Figure 2. For each of the two steady-state phases, four-time instances are investigated; one at the start, one at the end, and two in the middle of each phase. In contrast, the full duration of each of the three transient phases is examined. The grain recession is calculated at each burning step for the whole burning

time to be used in simulations representing the three transient phases and the eight points of steady-state phases computational domains.

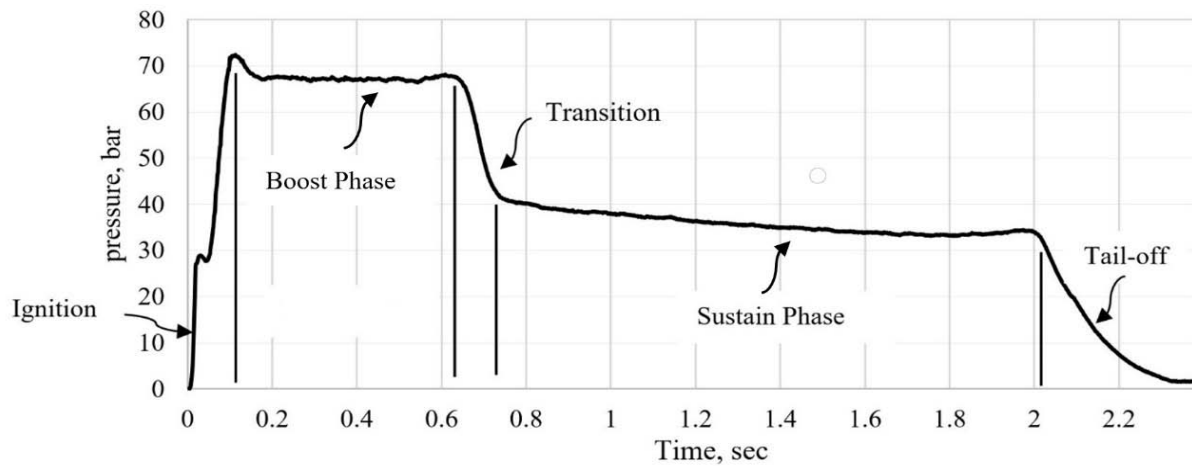


Figure 2: Pressure-time curve of the test rocket motor divided into regimes

The ignition phase represents the rise of the pressure from 0 to 71 bar in about 0.1 seconds, the boost phase of the test motor operation endures for about 0.5 seconds where pressure varies from about 71 to 68 bar. The transition represents the change from boost to sustain phase with a variation of pressure from 68 to 42 bar in 0.1 seconds. During the 1.12 seconds sustain phase, the motor pressure drops from 41 to 36 bar. Finally, the tail-off phase represents the collapse of pressure from 36 to 1 bar in about 0.33 seconds. The burning of propellant grain surfaces results in gases with direction normal to these surfaces, to simplify the problem, and as the pressure transducer is adjusted at the head end of the experimental motor, the simulation input (experimental pressure measurements) is adopted as pressure inlet.

a) Computational Domain

Due to grain regression during both boost and sustain phases, the computational domain geometry varies with time. Figure 3 shows the instantaneous grain locations calculated using the burning law (Equation 1) based on instantaneous chamber pressure values at five different times of burning. For more realistic simulations, the natural change of sharp corners into rounded ones upon regression is taken into consideration. The grain configuration at 0 seconds represents the computational domain for ignition phase transient simulation and boost start steady-state simulation. Grain location at 0.6 seconds represents the domain for boost-end steady-state simulation. Grain location at 0.75 seconds represents the domain for both sustain-start steady-state simulation and boost-sustain transition simulation. Grain location at 1.5 seconds is taken to define sustain-end steady-state simulation. For tail-off transient simulation, an empty chamber is considered.

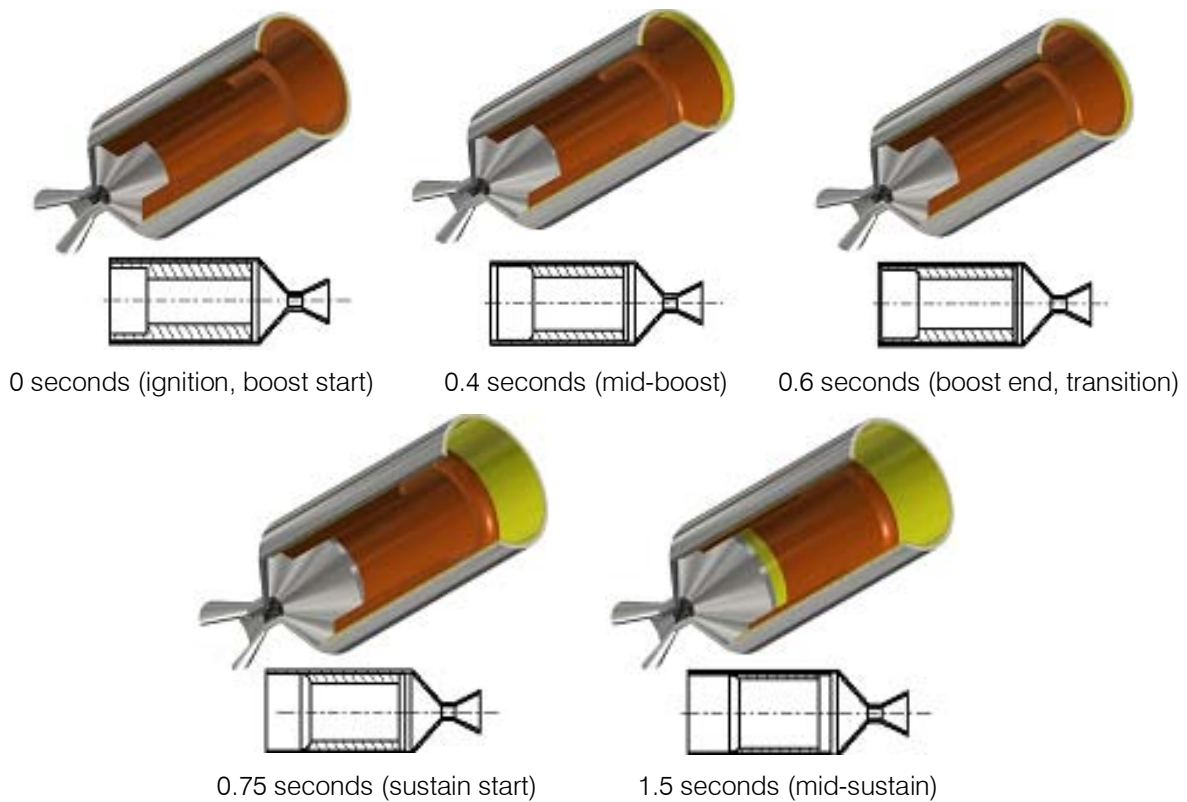


Figure 4: Grain configuration at the time instances in consideration

Due to the symmetry of flow and domain, two-dimensional axisymmetric computational domains are developed for all simulations. Multi-block structured grids are constructed such that grid quality is increased at areas of interest namely, solid walls, the nozzle critical section, and its upstream and downstream vicinity.

The mesh in the present work used structured grid element shape with appropriate number of divisions that suit each part of the motor. Spatial resolution is assessed through a grid independence check, the pressure at the throat was observed, and the grid-independent solution was obtained at 252000 cells. All wall boundaries in the domain are defined with the no-slip condition while the lower (bottom) boundary is defined as the axis. Consistent with experiments, the downstream (right) end of the domain is defined as a pressure outlet with atmospheric pressure definition. To simplify simulations, and since the pressure input to simulations is based on readings of a pressure transducer that is adjusted at the head end of the experimental motor, the upstream (left) end of the domain is defined as a pressure inlet as shown in Figure 5, which illustrate the mesh used in boost start steady case.

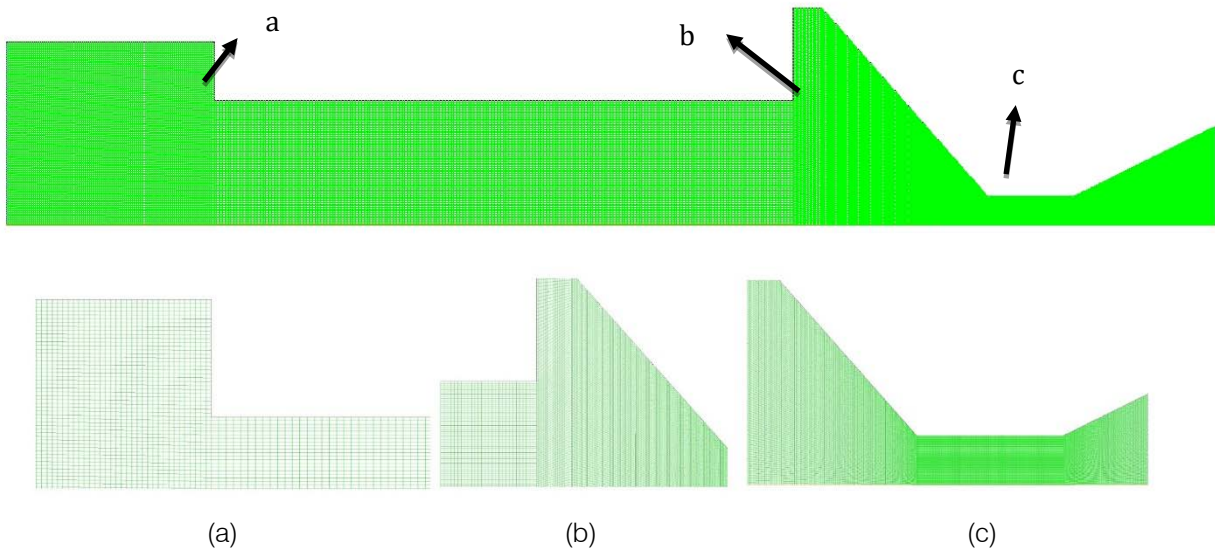


Figure 5: Mesh used in the boost start phase

b) Boundary Conditions

For the steady-state simulation, four main cases were selected to be discussed (boost-start, boost-end, sustain-start, and sustain-end), the instantaneous combustion pressures at the time instances in concern are set based on Figure 2. Hence, four steady cases correspond to inlet pressures of 71, 68, 41, and 36, respectively will be explained in detail in the current study. Another four cases are simulated, two in each steady phase to cover more points in the thrust curve and increase the prediction accuracy.

For transient phases simulations of Transition and Tail off, pressure inlet values are user-defined functions of time extracted from Fitted trendlines equations of the experimental curves illustrated in Figure 6, whereas in the ignition phase, the pressure-time relation is input as a table of discrete points (extracted from ignition experimental curve) within which instantaneous pressure value is interpolated.

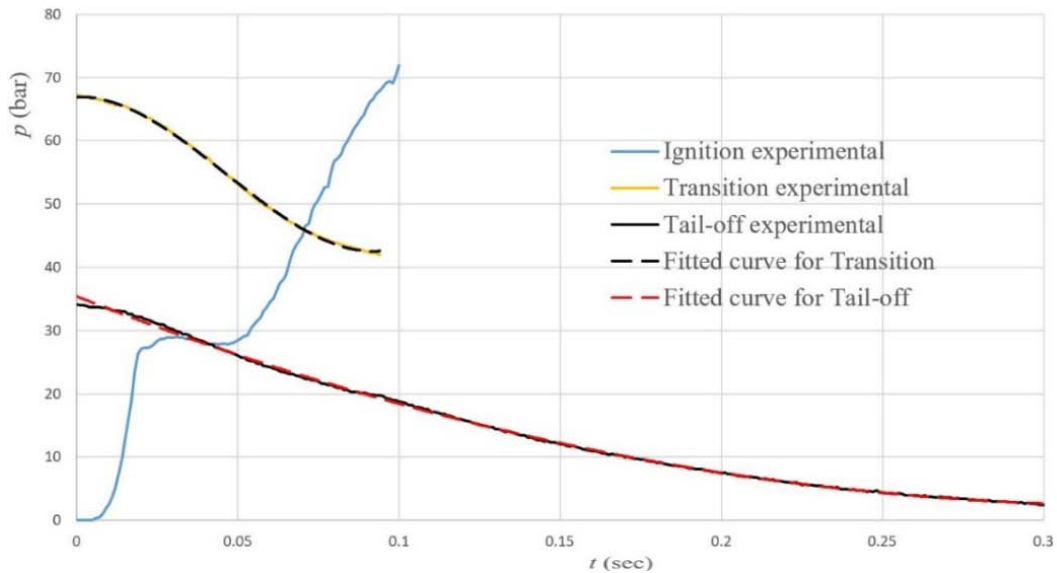


Figure 6: Temporal pressure variation of pressure inlet boundary for transient phases simulations

For boost-sustain and tail-off transient phases' simulations, the experimental pressure-time curve data is analyzed and equations of the fitted curves (polynomial equations of trendlines) are used in the user-defined function input files. These functions are:

Transition phase: $p = 64830t^3 - 9029.6t^2 + 16.745t + 66.935$ (2)

Tail-off phase: $p = 303.9t^2 - 200.28t + 35.408$ (3)

where p is the inlet pressure value in bar while t represents the time in seconds.

c) *Operating Fluid Properties*

Properties of working gas adopted in CFD solver setup are sought to be as close to real combustion as possible. This is done by conducting thermochemical calculations using NASA CEA [28] code. It is one of the thermochemical programs that are capable of calculating the chemical equilibrium compositions of a chemical system via minimization of free energy formulation, which allows one to calculate theoretical thermochemical properties. Combustion

pressure is input as well as ingredients of solid propellant (listed in Table 1) as reactants in the form of weight percentage along with enthalpy, temperature, and chemical formula of each. Grain burning is considered a finite area combustion problem with a contraction ratio (ratio of finite chamber area to throat area) of 7.475 and an initial chamber temperature guess of 3800k. Table 2 lists the operating gas properties for all steady cases in boost and sustain phases.

Table 2: Operating gas properties as calculated by NASA CEA

Simulation Case Parameter	Boost start	Boost end	Sustain start	Sustain end
Camber pressure (bar)	71	68	41	36
Temperature (K)	3388	3385	3344	3332
Density (kg/m ³)	6.9038	6.6119	3.9767	3.4868
Specific heat (J/kg.K)	3547.3	3568.7	3836.2	3910.1
Thermal conductivity (w/m.K)	1.0381	1.0467	1.1554	1.1856
Viscosity (kg/m.s)	9.88 e-05	9.87e-05	9.7925e-05	9.769e-05
Specific heat ratio	1.1411	1.1409	1.1378	1.1370
Specific gas constant (J/K.mol)	323.27	323.397	324.78	325.15

d) *CFD Solver Setup*

The pressure-based solver for Navier-Stokes equations is adopted. For the pressure-velocity-coupling scheme, the pressure-based coupled algorithm is chosen as it gives a more efficient, accurate, and robust single-phase implementation in cases of steady-state flows. Turbulence is modeled in Reynolds-Averaged Navier-Stokes (RANS) through the standard $k-\epsilon$ model. It is preferred because of its reasonable accuracy and reliability for a wide range of turbulent flows and heat transfer. It is thus the most commonly used turbulence model, especially with solid rocket motors cases [29-33]. Gradients are computed in the current work using the Least-square cell-based method while the PRESTO discretization scheme is chosen as it is more suitable for multiphase simulations. For unsteady simulation cases, the time step size in each case is chosen to be compatible with the input file data based on a temporal resolution sensitivity check. The working fluid is chosen as an ideal gas with the specifications tabulated in Table 2.

two sections, transient phases, and steady-state phases.

a) *Transient Phases*

Figure 7 (a, b, c, and d) shows the flow velocity streamlines along the motor at different times of the ignition phase colored according to velocity values, Figure 6.a shows the whole motor with nozzle, whereas the other figures focus on the velocity streamlines variation inside the combustion chamber. Vortices can be noticed inside the combustion chamber at the beginning of ignition, especially in the gap between grain and nozzle. These vortices seem to diminish or vanish with time as the pressure becomes high enough to make the flow smoother. The flow parameters change along the motor at different times of ignition are shown in Figure 8 where flow pressure and velocity along the axis are displayed. Flow pressure has a high, nearly constant, value inside the combustion chamber and these values decrease along the nozzle at all times of ignition. In contrast, velocity is nearly zero inside the chamber and then increases along with the nozzle. It can be noticed that the flow doesn't fully expand along the nozzle at the beginning of ignition where the pressure value inside the combustion chamber is still not high enough.

During the transition phase, the pressure drops sharply while the grain almost maintains its

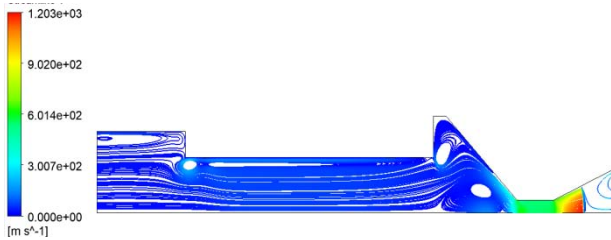
IV. DISCUSSION OF INTERNAL BALLISTICS SIMULATION RESULTS

Results of numerical simulation for the flow inside the test motor in concern are discussed below in

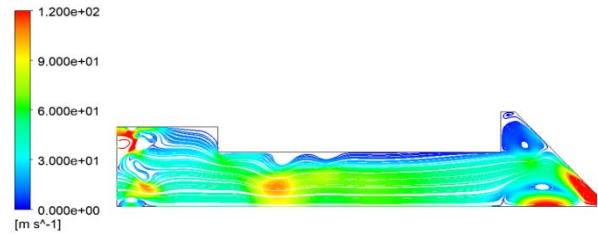
configuration. The velocity streamlines variation at different times of transition phase time is shown in Figure 7 (e, f, g, and h). It can be noticed that the flow streamlines as it transfers from the boost phase with high pressure to the sustain phase with lower pressure become smoother. The recirculation bubbles along the motor diminish in number and size. The flow parameters along the motor at different times of this phase are shown in Figure 8. Pressure has a higher value inside the combustion chamber and decreases along the nozzle at all times of burning. The flow velocity inside the

combustion chamber has a low value that increases along the nozzle.

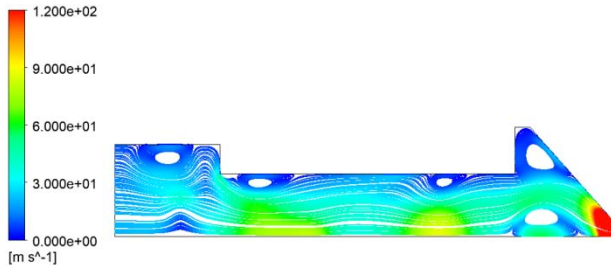
The tail-off phase represents about 0.3 seconds of motor operation. Figure 7 (i, j, k, and l) shows the variation of flow streamlines colored according to velocity values. Over time, the velocity decrease as the pressure inside the combustion chamber is relieved and the streamlines vortices still exist inside the empty motor. The flow parameters along with the motor at different times of this phase are shown in Figure 8.



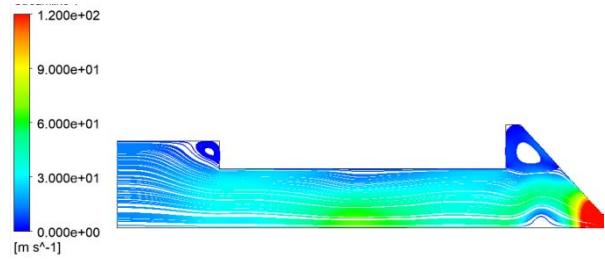
(a) 0.002 seconds of ignition



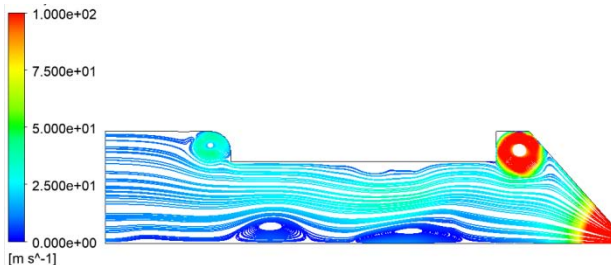
(b) 0.006 seconds of ignition



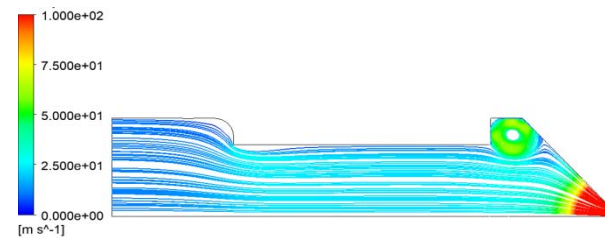
(c) 0.04 seconds of ignition



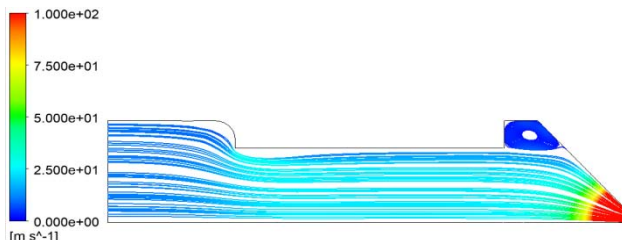
(d) 0.1 seconds of ignition



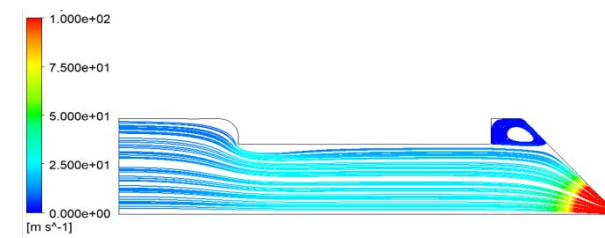
(e) 0.006 seconds of transition



(f) 0.017 seconds of transition



(g) 0.04 seconds of transition



(h) 0.095 seconds of transition



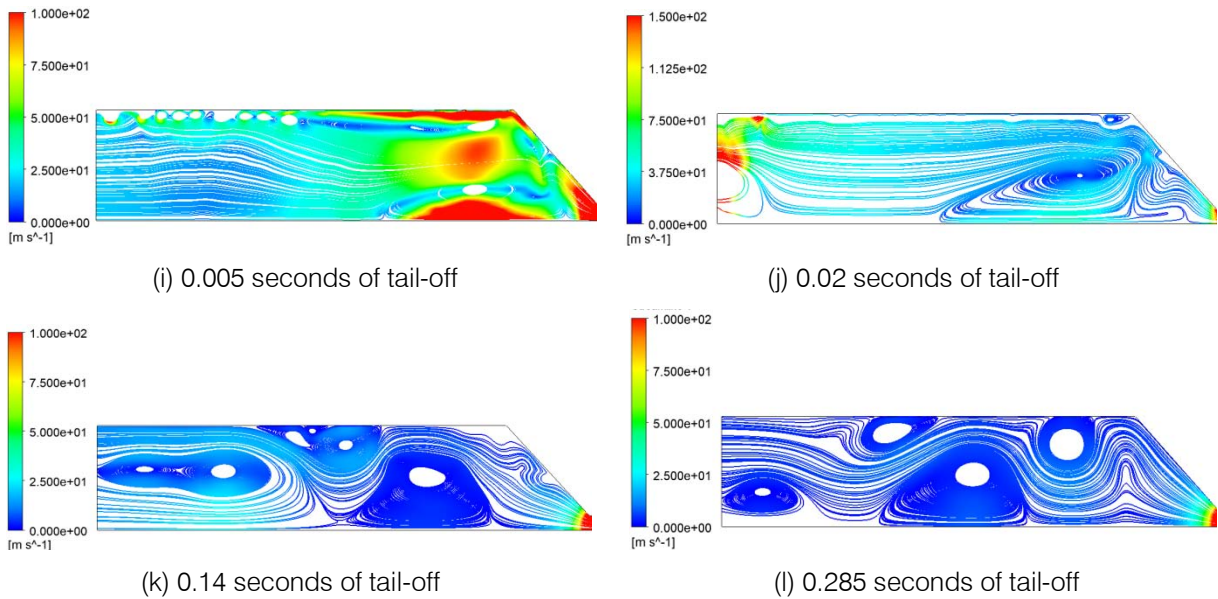


Figure 7: Flow streamlines at different time instances during transient phases

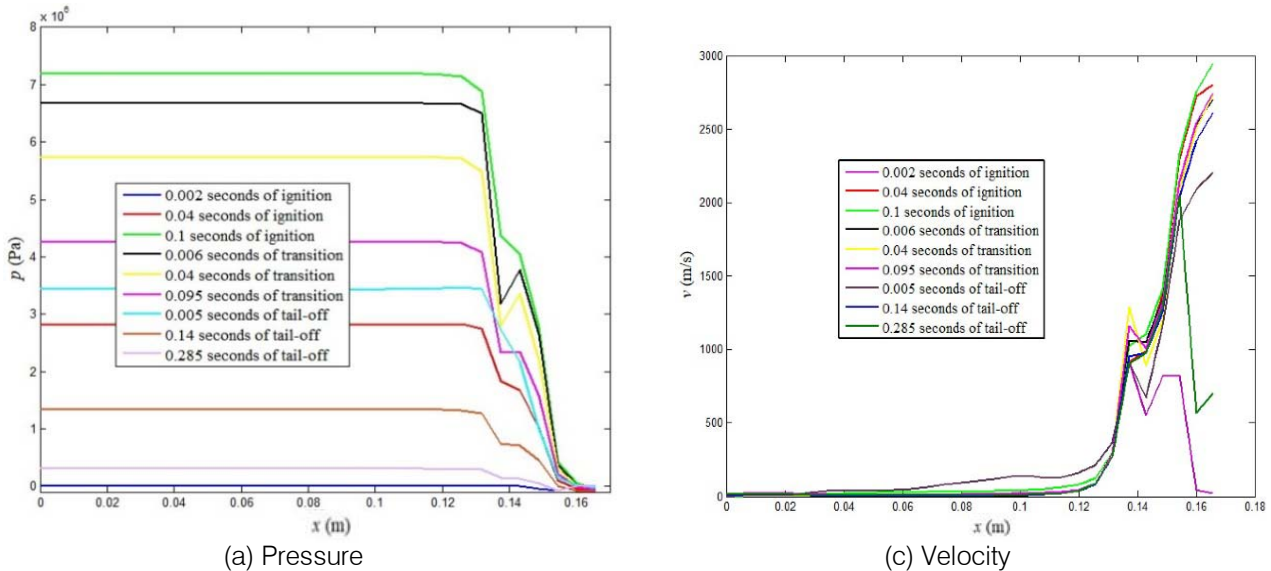


Figure 8: Variation of Pressure (left side) and Velocity (right side) along the motor axis at different times of the transient phases

b) Steady State Cases

Four steady-state simulation cases are considered for each phase, the simulation results are presented in detail for two cases at each phase namely; at its start and end. Figure 9 illustrates pressure contours along with the motor for two cases in the boost phase and two cases in the sustain phase. The first case includes the whole motor, while the other three cases focus on the combustion chamber as the pressure values are higher inside it. The pressure clouds concentrate in the middle of the motor and close to the convergent part, the pressure values are higher in the center of these clouds. In addition, the variation of gases pressure and Mach Number along the motor axis

at the start and end of each steady phase is illustrated in Figure 10.

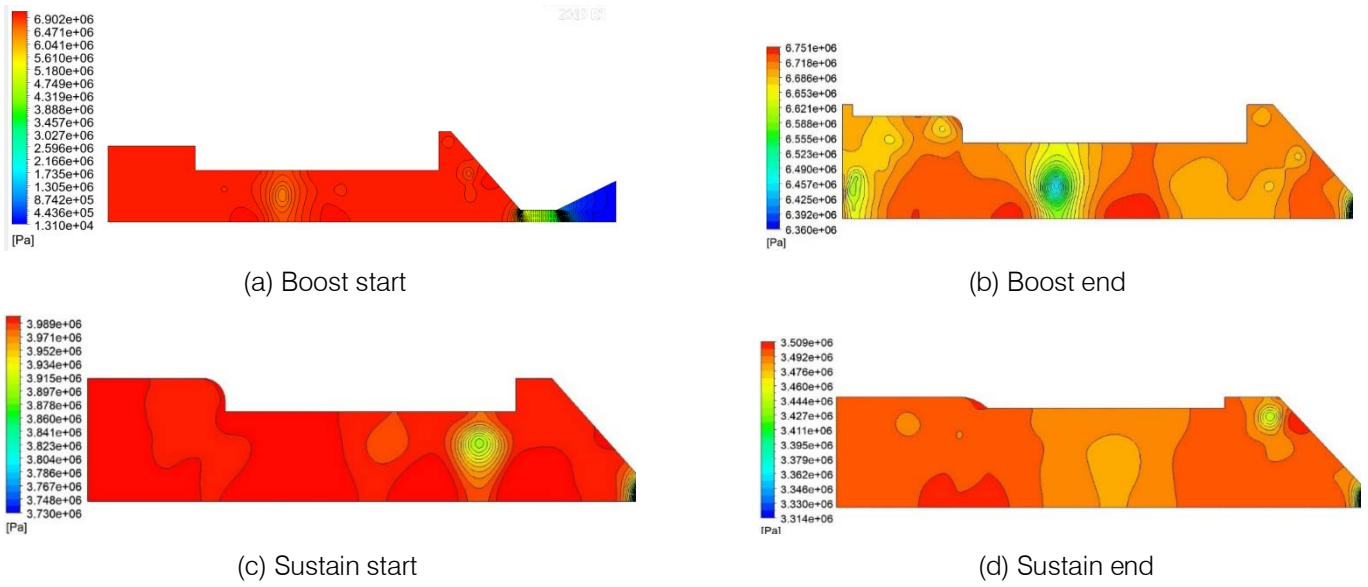


Figure 9: Pressure contours at the start and end of each steady phase

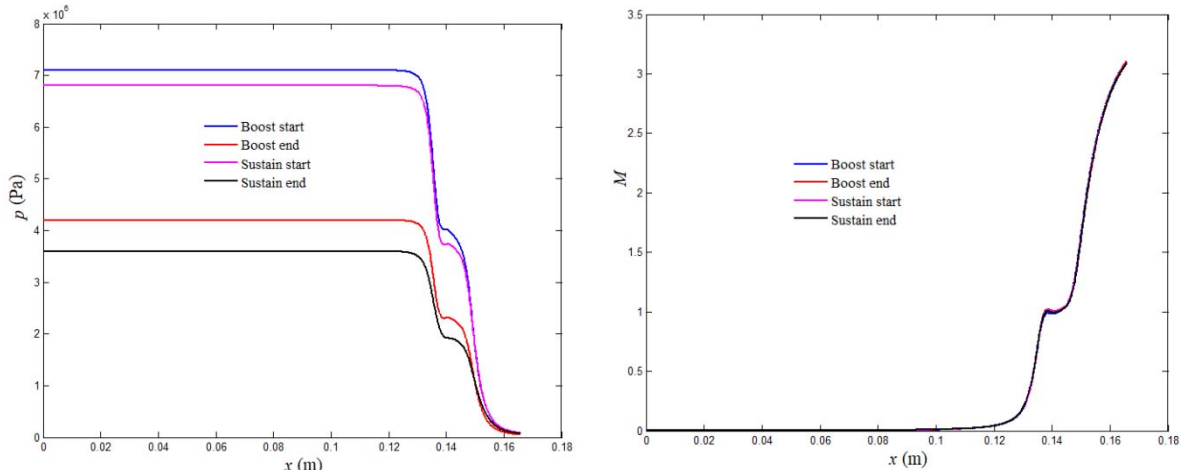


Figure 10: Variation of Pressure (left side) and Mach Number (right side) along the motor axis at the start and end of each steady phase

The pressure at the combustion chamber is high and starts to decrease once it enters the nozzle and continues decreasing as the flow passes through the nozzle divergent section until it reaches the atmospheric value at exit. In contrast, the Mach number starts to rise above zero at the nozzle inlet, reaches the value of one at the nozzle throat, and above 3 at the nozzle exit. Flow properties vary in the radial direction as well. Figure 11 shows the variation of flow pressure and Mach number with radius along the nozzle exit. While pressure reaches a maximum value midway along the nozzle radius in boost phase cases, it reaches a maximum value near the walls in sustain phase cases. Mach value drops sharply inside the boundary layer over the wall, for the boost phase cases it decreases to 2 while for the sustain phases it reaches 0.5.

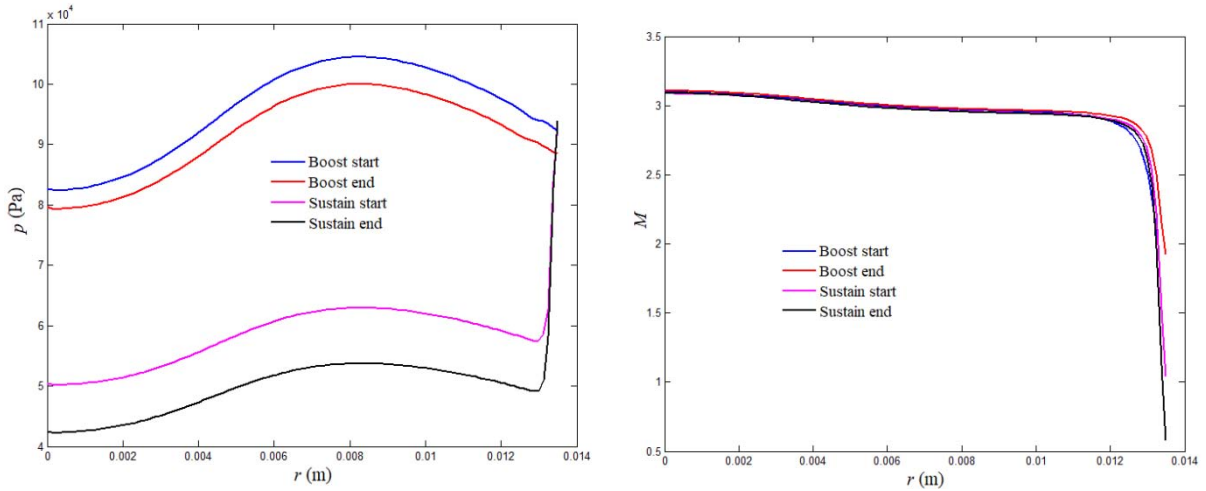


Figure 11: Variation of Pressure (left side) and Mach Number (right side) along the motor exit

Year 2023

V. VALIDATION OF THRUST CALCULATION

An analytical model was developed based on dividing the web thickness into segments, a solution of the governing equation for each segment is performed, and a comparison is made to check whether the total mass generated from grain burning equals the total mass discharged from the nozzle [34]. The model was adopted to calculate the thrust for the used motor. The root mean square error between analytical calculations and experimental measurements is about 15% as shown in Figure 12. The error was estimated based on the difference between the thrust values calculated analytically and experimentally measured. The root mean square of the difference is the error represented in the current method.

The thrust based on the numerical simulation is calculated using the flow properties calculated at the exit section of the nozzle via the following equation [35]:

$$F = \dot{m} V_e + A_e(P_e - P_a) \tag{4}$$

where \dot{m} is the mass flow rate discharged from the motor nozzle exit, V_e is the average velocity in this area, A_e is the surface area of the exit section, P_e is the average exit pressure, and P_a is the atmospheric pressure (101325 Pascal). The calculated values of these parameters for the four steady-state cases examined here are listed in Table 3, beside the main four points, two in each phase to cover the curve. The thrust values calculated using the numerical simulation are compared with thrust experimental measurements, Figure 12.

Table 3: Numerical parameters used in thrust calculations for main steady phases

	Boost-start	Boost-end	Sustain-start	Sustain-end
Mass flow rate (kg/sec)	0.1896	0.18095	0.1114	0.09799
Exit pressure (Pascal)	95734.06	90775.95	57962.66	50508.6
Exit velocity (m/sec)	2806	2804	2806	2804



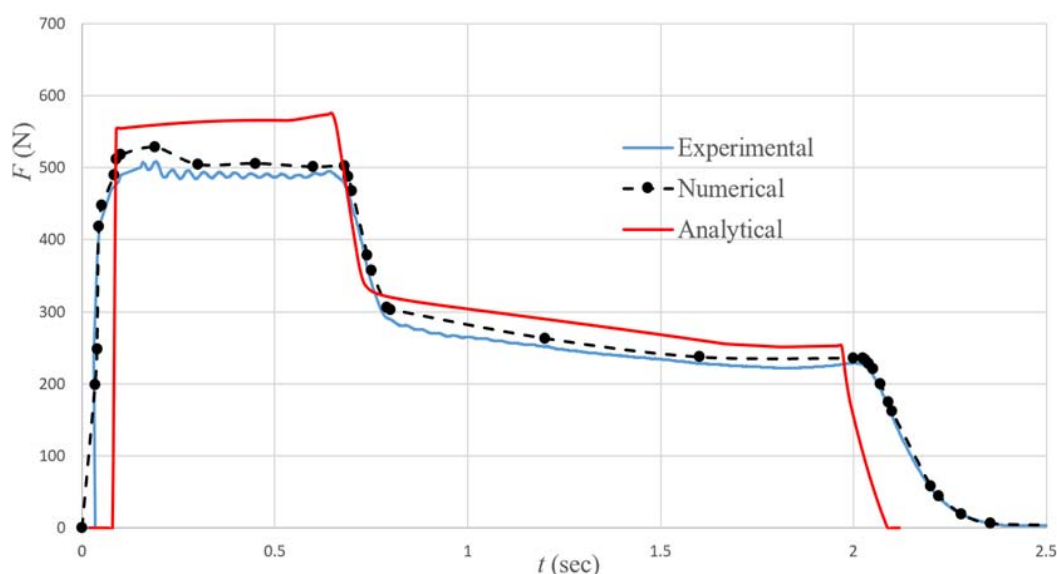


Figure 12: Experimental vs Numerical and Analytical thrust ~ time curves

The numerical simulation values are in a marginal similarity to measured values with a relative error of less than 5% whereas the analytical calculation can predict the thrust with an accuracy of about 15% relative to the experimental measurements. The deviation between the numerical simulation and the experimental measurements in the transient phases is less than the deviation in the boost and sustain phase, this is due to the relative error occurring during burnback calculation analysis in the boost and sustain phase, but in the transient phases, the grain burn back process doesn't exist. It can be concluded from this comparison that numerical simulations are capable of calculating thrust using measured pressure as an alternative to thrust measurements.

VI. CONCLUSION

An experiment-based numerical simulation and analysis for a dual thrust solid-propellant motor was carried out to investigate the flow features and parameters along the motor and nozzle for the whole working time. This gives more understanding and better insight that cannot be accomplished with experimental measurements. The pressure-time curve from experimental measurements was analyzed to obtain the inputs required for the simulations whereas gas parameters were calculated from thermochemical calculations. The pressure-time curve was divided into two types of simulation, steady-state and transient, the steady-state phase was represented in two phases, boost phase and sustain phase steady-state simulations. The transient phases were represented in three phases, ignition phase, transition (from boost to sustain) phase, and tail off phase. The results from numerical simulation were used to calculate the motor thrust via using the parameters marched out from the

motor exit. The thrust values calculated from numerical simulations were compared with the experimental measurements and the error was less than 5% in all cases. Numerical simulations were confirmed capable of explaining the flow parameters variations with time as well as calculating the motor thrust with a remarkable level of accuracy compared with analytical calculations that are more suited for preliminary calculations.

REFERENCES RÉFÉRENCES REFERENCIAS

1. Blazek J. Flow simulation in solid rocket motors using advanced CFD. 39th AIAA/ASME/SAE/ASEE Joint Propulsion Conference and Exhibit. 2003; 5111.
2. Hartfield RJ, DiMaggio GA, Majdalani J. Efficient Solution Approach for Internal Ballistics. AIAA Propulsion and Energy 2020 Forum. 2020; 3926.
3. Ramesh Kumar R, Devarajan Y. CFD simulation analysis of two-dimensional convergent-divergent nozzle. International Journal of Ambient Energy 2020; 41(13):1505-15.
4. Najar NA, Dandotiya D, Najar FA. Comparative analysis of $k-\epsilon$ and spalart-allmaras turbulence models for compressible flow through a convergent-divergent nozzle. The International Journal of Engineering Science 2013; 2(8):8-17.
5. Tanveer N, Mohanraj C, Jegadeesan K, Maruthupandiyar S. Comparative studies on various turbulent models with liquid rocket nozzle through computational tool. Advanced Materials Research. 2014; 1204-9.
6. Kostić O, Stefanović Z, Kostić I. CFD modeling of supersonic airflow generated by 2D nozzle with and without an obstacle at the exit section. FME Transactions 2015; 43(2):107-13.

7. Dang Le Q, Mereu R, Besagni G, Dossena V, Inzoli F. Computational fluid dynamics modeling of flashing flow in convergent-divergent nozzle. *Journal of Fluids Engineering* 2018; 140(10):1-22.
8. Natta P, Kumar VR, Rao YH. Flow analysis of rocket nozzle using computational fluid dynamics (CFD). *International Journal of Engineering Research Applications* 2012; 2(5):468-71.
9. Ajith S, Nichith C, Vignesh S, et al. 3D Flame Spread and Starting Transient in Dual-thrust Solid Propellant Rocket Motors. 52nd AIAA/SAE/ASEE Joint Propulsion Conference. 2016; 4598.
10. Sanal Kumar V, Ramesh kumar T, John J, Basavanahalli R. 3D Flow Simulation of Dual Thrust Solid Rocket Motors during Starting Transient. 50th AIAA/ASME/SAE/ASEE Joint Propulsion Conference. 2014; 3807.
11. Chandrasekaran N, Sankar V, Nejaamtheen MN, Selvakumar K, Rahman SA, Sanal Kumar V. Analytical and Numerical Predictions of Boundary Layer Blockage in Dual Thrust Motors. 2018 Joint Propulsion Conference. 2018; 4880.
12. Ajith S, Mani S, Tharika R, Nagaraju Doddi H, Sanal Kumar V. Diagnostic investigation of flame spread mechanism in dual-thrust solid propellant rocket motors. 51st AIAA/SAE/ASEE Joint Propulsion Conference. 2015; 4226.
13. Chandrasekaran N, Sankar V, Padmanabhan S, et al. Studies on Oscillating Boundarylayer During the Ignition Transient of Dual-thrust Solid Rocket Motors. 53rd AIAA/SAE/ASEE Joint Propulsion Conference. 2017; 4691.
14. Cho IH, Baek SW. Numerical simulation of axisymmetric solid rocket motor ignition transient with radiation effect. *Journal of Propulsion and Power* 2000; 16(4):725-8.
15. Ropia B, Shekhar HK, Thakur DG. Study of Initial Pressure Rise in Multi Grain Solid Propellant Rocket Motor. *Propellants, Explosives, Pyrotechnics* 2020; 45(5):741-50.
16. Bianchi D, Grossi M, Favini B, Serraglia F, Ierardo N. Analysis and Reconstruction of Zefiro 40 Solid Rocket Motor Static Firing Tests and Extrapolation to Flight. *AIAA Propulsion and Energy 2021 Forum*. 2021; 3703.
17. Tengli PN, Ramesh C, Viswanathan K, Saravanan. Vortex flow analysis of a large segmented solid rocket motor. *Indian Journal of Science and Technology* 2012; 5(1):1888-92.
18. Chen L, Gao Y, Wang D, Zou Q, Zhang S. Numerical simulation on acoustic mode and pressure-oscillation decay in finocyl-and axil-grain combustion chambers. *Aerospace Science and Technology* 2020; 107:106351.
19. French AD, Panelli M, Di Lorenzo G, Schettino A, Paglia F. Combustion instability and Pressure oscillation numerical simulation in a solid rocket motor. 53rd AIAA/SAE/ASEE Joint Propulsion Conference. 2017; 4952.
20. Ji S, Wang B, Zhao D. Numerical analysis on combustion instabilities in end-burning-grain solid rocket motors utilizing pressure-coupled response functions. *Aerospace Science and Technology* 2020; 98:105701.
21. Di Mascio A, Cavallini E, Favini B, Neri A. Numerical Simulation of 3D Unsteady Flowfield in Aft-Finocyl Solid Rocket Motor. 50th AIAA/ASME/SAE/ASEE Joint Propulsion Conference. 2014; 4015.
22. Pengfei R, Hongbo W, Guofeng Z, et al. Solid rocket motor propellant grain burnback simulation based on fast minimum distance function calculation and improved marching tetrahedron method. *Chinese Journal of Aeronautics* 2021; 34(4):208-24.
23. Li Q, He G-q, Liu P-j, Li J. Coupled simulation of fluid flow and propellant burning surface regression in a solid rocket motor. *Computers and Fluids* 2014; 93:146-52.
24. Qingyu L, Kun J, Hao W, Jinlong W. Application of immersed boundary method to the simulation of transient flow in solid rocket motors. *Aerospace Science and Technology* 2021; 1.310:1-14.
25. Zou X, Wang N, Han L, Bai T, Xie K. Numerical investigation on regression rate and thrust regulation behaviors of a combined solid rocket motor with aluminum-based fuel. *Aerospace Science and Technology* 2021; 119:107102.
26. Han S, Kim C. Integrated Fluid-Structure Simulation for Full Burning of a Solid-Propellant Rocket Interior. *Journal of Propulsion and Power* 2014; 30(4):883-900.
27. Hemanth VA, Jyothi U. CFD Analysis of a Solid Propellant Retro Rocket Motor using Ansys Fluent. *International Conference on Design and Manufacturing aspects for Sustainable Energy*. 2020; 01054.
28. McBride BJ. NASA Glenn coefficients for calculating thermodynamic properties of individual species: National Aeronautics and Space Administration, John H. Glenn Research Center at Lewis Field, 2002.
29. Biju Kuttan P, Sajesh M. Optimization of divergent angle of a rocket engine nozzle using computational fluid dynamics. *The International Journal Of Engineering And Science* 2013; 2(2):196-207.
30. Thakre P, Rawat R, Clayton R, Yang V. Mechanical erosion of graphite nozzle in solid-propellant rocket motor. *Journal of Propulsion and Power* 2013; 29(3):593-601.
31. Yumuşak M. Analysis and design optimization of solid rocket motors in viscous flows. 21st AIAA Computational Fluid Dynamics Conference 2013; 75:22-34.
32. Li Z, Xiang H, Zhang JT. Numerical simulation of composite solid propellant rocket motor exhaust

- plume. Journal of Solid Rocket Technology 2014; 37(1):37-42.
33. Belega B-A, Nguyen TD. Analysis of flow in convergent-divergent rocket engine nozzle using computational fluid dynamics. International Conference of Scientific Paper. 2015.
 34. Gawad ARA, Mohamed MY, Abdalla HM, Elsenbawi MA. Analytical Prediction of Dual-Thrust Rocket motors under Uncertainties. 16th International Conference on Aerospace Sciences & Aviation Technology , ASAT - 16 2015.
 35. Sutton GP, Biblarz O. Rocket propulsion elements: John Wiley & Sons, 2016.

